

advances.sciencemag.org/cgi/content/full/6/20/eaaz5093/DC1

Supplementary Materials for

From force-responsive molecules to quantifying and mapping stresses in soft materials

Yinjun Chen, C. Joshua Yeh, Yuan Qi, Rong Long, Costantino Creton*

*Corresponding author. Email: costantino.creton@espci.fr

Published 15 May 2020, *Sci. Adv.* **6**, eaaz5093 (2020)

DOI: [10.1126/sciadv.aaz5093](https://doi.org/10.1126/sciadv.aaz5093)

This PDF file includes:

Schemes S1 and S2

Tables S1 to S3

Figs. S1 to S12

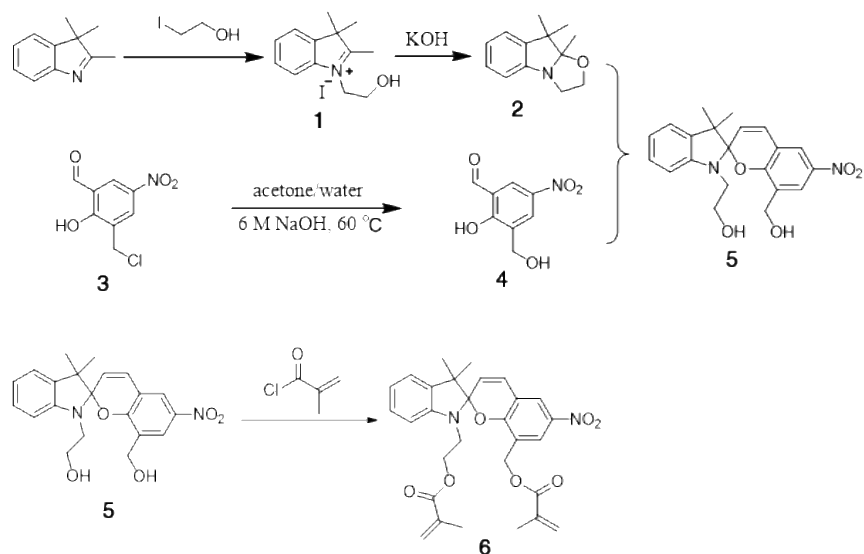
1 Materials synthesis

Materials: All reagents, including chemical products, solvents and monomers, were purchased from Sigma-Aldrich and VWR and used as received except the monomers. All the monomers (ethyl acrylate, EA) and crosslinker were purified by a chromatography column of activated alumina to remove the inhibitor. Then the monomers were degassed by nitrogen gas and stored in a glove box.

General methods: NMR spectra were measured at room temperature by a 400 MHz Bruker Avance II 400 spectrometer. Uniaxial extension and fracture tests were performed on a standard tensile Instron machine, model 5565 with a 100 N load cell. All the videos used to record the uniaxial extension and fracture tests were carried out with an RGB camera (SONY IMX 174, STC-MCS241U3V).

1.1 Synthesis of spiropyran-diene

Spiropyran-diol was synthesized following a previously reported protocol (12-14) and the detailed process is shown in Scheme . To use spiropyran-diol as a crosslinker in a free radical polymerization, the diol was modified to a diene by using methacryloyl chloride. First, SP-diols (250 mg, 0.65 mmol, 1.0 eq.) and triethylamine (907 μ L, 6.5 mmol, 10 eq.) were dissolved in 30 mL tetrahydrofuran. The solution was mixed in an ice bath for 15 min. Subsequently, methacryloyl chloride was added into the solution. The color of the solution was observed to change from purple to yellow. Then, the temperature of the reactor was increased to room temperature in 3 hours. After 24 hours, some pink precipitate was generated at the bottom of flask and the solution color turned pink. The solvent was evaporated under vacuum after filtration. The raw product was dissolved into 50 mL of dichloromethane and the solution was washed three times with a saturated K_2CO_3 aqueous solution. Then, dichloromethane was removed and a purple paste was obtained. To purify the SP-diene, a column chromatography of silica was used with dichloromethane as the eluent. Three compositions flowed out from the column, where SP-diene was the middle one. The SP-diene solution was collected and the solvent was removed under vacuum. Recrystallization in n-hexane was used to further purify the SP-diene. Finally, a pure product of yellow powders (223 mg, 0.43 mmol, 66%) was obtained.



Scheme S1: Synthesis of spiropyran-diene.

The NMR spectrum of spiropyran-diene is shown in Figure S1 and the detailed analysis of the spectrum is as follows: ^1H NMR (400 MHz, CDCl_3) δ 8.09 (s, 1H), 7.98 (s, 1H), [7.19-6.66] (m, 5H), 6.05 (s, 2H), [5.91&5.88] (d, 1H), 5.57 (m, 2H), 4.97 (s, 2H), [4.31-4.27] (t, 2H), [3.57-3.37] (m, 2H), 1.91 (m, 3H), 1.27(s, 6H),

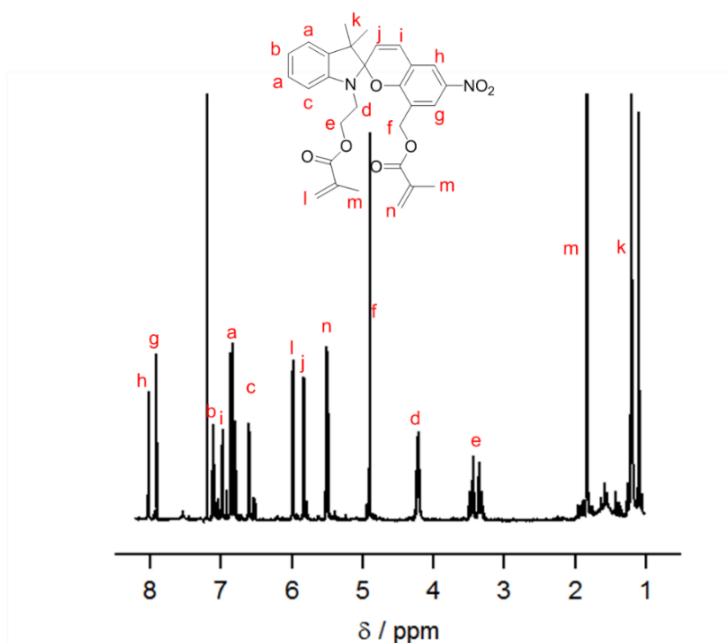
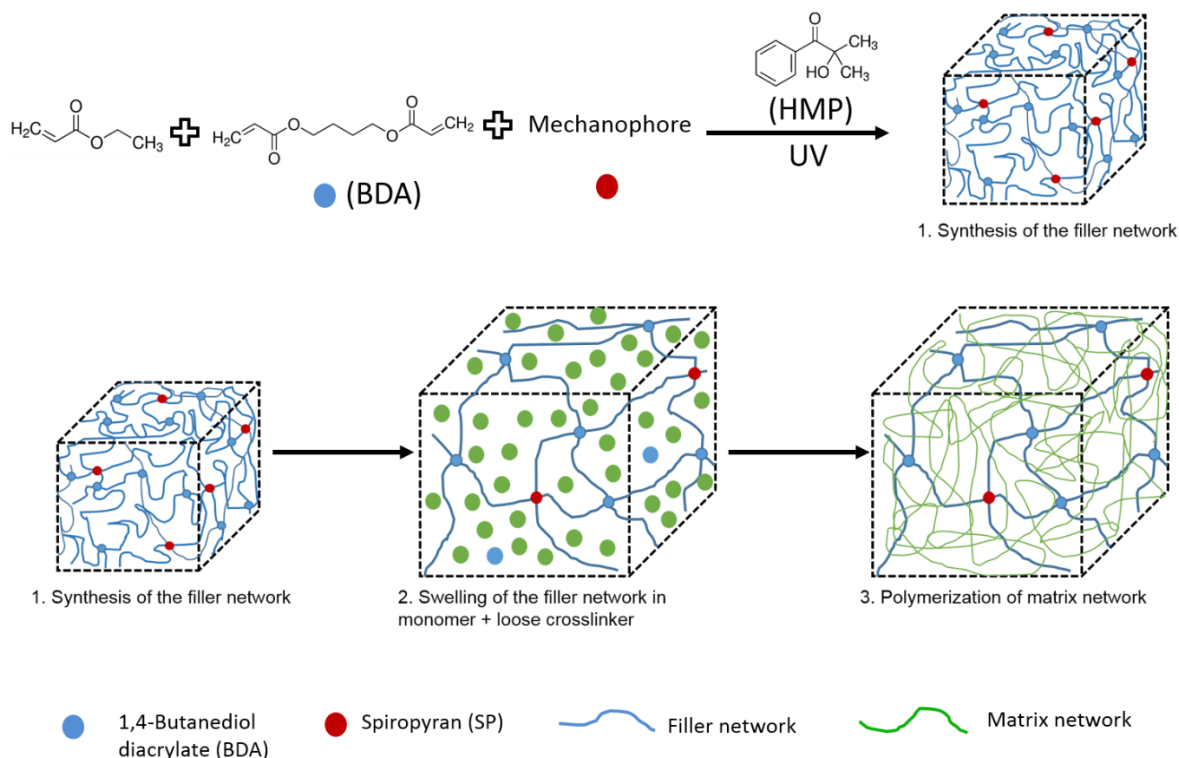


Figure S1: NMR spectra of spiropyran-diene.

1.2 Fabrication of multiple network elastomers

The detailed synthesis of multiple networks was similar to what was reported in a previous publication by Ducrot et al. (19,28,29) SP was covalently incorporated into the first network along with BDA. To accomplish this, 1 mol% 2-hydroxy-2-methylpropiophenone (HMP) UV initiator, 0.5 mol% cross-linker (0.05 mol% SP and 0.45 mol% BDA) was dissolved into ethyl acrylate (EA), resulting in a purple pre-gel solution. Note that molar percentages are with respect to moles of EA. The solution was poured into a mold composed of two glass plates with a silicone spacer to control the film thickness. The whole device was tightened by two metal frames to seal the mold. Polymerization was initiated by UV light (by a Vilbert Lourmat lamp: model VL-215.L). After polymerization, a uniform purple rubbery single network was formed and subsequently dried in a vacuum desiccator for one day to remove unreacted monomers. After drying, the single network exhibited a reddish color and was stored at room temperature in a dark environment for later use.

The multiple networks were prepared by sequential swelling and polymerization as shown in Scheme S. A small piece (about 3 cm length and 2 cm width) of the single network (SN) with mass (m_{SN}), was cut out from the first network film and soaked in a solution containing dilute BDA cross-linker (0.01 mol/% respective to EA), 0.01 mol/% HMP, and EA. When equilibrium swelling was reached after 2 hours, double networks (DN) were synthesized by UV polymerizing the swollen single network. After drying in a vacuum desiccator, the sample appeared colorless and its mass (m_{DN}) was measured. The two steps (swelling and polymerization) were repeated on the DN to prepare triple networks (TN).



Scheme S2: Synthetic procedure of multiple network elastomers. The green, blue and red dots respectively represent EA monomers, BDA and SP crosslinkers. The blue and green lines correspond to the polymer chains of poly(ethyl acrylate) in the filler network and matrix network, respectively.

As a reference, another SN with a different cross-linker density at a fixed SP concentration was synthesized. The cross-link density was varied from 0.5 mol% to 0.2 mol% relative to monomer. Based on this SN, another family of materials (EA0.2-0.05) including DN and TN were synthesized as shown in Table S1.

In order to study the effects of SP concentration on the color change, it is necessary to prepare elastomers possessing identical (or at least very similar) mechanical properties. Because the mechanical properties are controlled by the first network, the cross-linking density in the first network was kept constant, but the ratio between SP mechanophore crosslinker and BDA crosslinker was varied. A series of single networks were synthesized and the respective double and triple networks were also prepared as shown in Table S1. The synthesized process was the same as the description above.

Table S1: Summary of materials composition

Sample name	BDA in 1 st network (mol%)	SP in 1 st network (mol%)	1 st network wt%	2 nd network wt%	3 rd network wt%	N _{poly}	λ_0
EA0.5-0.05(1)	0.45	0.05	100	0	0	1	1
EA0.5-0.05(1.56)	0.45	0.05	26.5	73.5	0	2	1.56
EA0.5-0.05(2.23)	0.45	0.05	9.0	25	66	3	2.23
EA0.2-0.05(1)	0.15	0.05	100	0	0	1	1
EA0.2-0.05(1.70)	0.15	0.05	20.2	79.8	0	2	1.70
EA0.2-0.05(2.61)	0.15	0.05	5.6	22.1	72.3	3	2.61
EA0.5-0.025(1)	0.475	0.025	100	0	0	1	1
EA0.5-0.025(1.60)	0.475	0.025	24.3	75.7	0	2	1.6
EA0.5-0.025(2.35)	0.475	0.025	7.8	24.2	68	3	2.35
EA0.5-0.0125(1)	0.4875	0.0125	100	0	0	1	1
EA0.5-0.0125(1.58)	0.4875	0.0125	25.3	74.7	0	2	1.58
EA0.5-0.0125(2.36)	0.4875	0.0125	7.6	22.5	70	3	2.36

2 Mechanical testing

2.1 Uniaxial tensile tests

Uniaxial extension experiments were performed on a standard tensile Instron machine, model 5565, fitted with a 100 N load cell and custom pneumatic clamps. The clamps reduced slippage and damage to the samples by allowing precise control over clamp pressure. For uniaxial tensile tests, samples with a dog-bone shape were made by using a pre-made punch. The gauge length of the central part is about 20 mm and the thickness of samples varied from 0.6 to 2 mm. Tests were performed with a nominal stretch rate $\dot{\lambda}$ of 0.05 s^{-1} . To measure the strain during the uniaxial deformation, two black marks were made on the homogeneously deformed zone of the specimens. An RGB camera (SENTECH: STC-MCS241U3V, image sensor: SONY IMX174, cell size: $5.86 \mu\text{m} \times 5.86 \mu\text{m}$) with a frame rate of 25 fps was used to record the relative displacement of the two black markers. MATLAB scripts were used to analyze the position of the marks from the recorded videos, which allowed for accurate determination of the locally applied uniaxial stretch. The nominal extension ratio was defined as:

$$\lambda = \frac{L}{L_0} \quad \text{Eq. S1}$$

where L_0 and L are the distances between the two centroids of the marks before and after stretching, respectively. The engineering stress was obtained from the Instron machine. Before performing tensile tests, all specimens were exposed to white light for 5 mins to ensure that all of the mechanophores were in its inactivated SP form. To study the mechanical properties of interpenetrated multiple network elastomers, tensile tests with various polymer networks were carried out. First, to examine the effects of incorporating SP as a crosslinker, diverse single networks with 0.5 mol% cross-linker density were synthesized. Figure S2a shows stress-strain curves of networks with varying SP concentrations at the same total crosslinker concentration. No significant differences in the stress-strain response were observed in the single networks. Thus, the incorporation of SP does not affect the mechanical properties of SNs, indicating that SP can be used as a molecular probe for the measurement of stress in elastomers. Due to the similar mechanical properties of the first network, the DNs and TNs containing SP did not show obvious differences compared with a control sample (without SP in the first network).

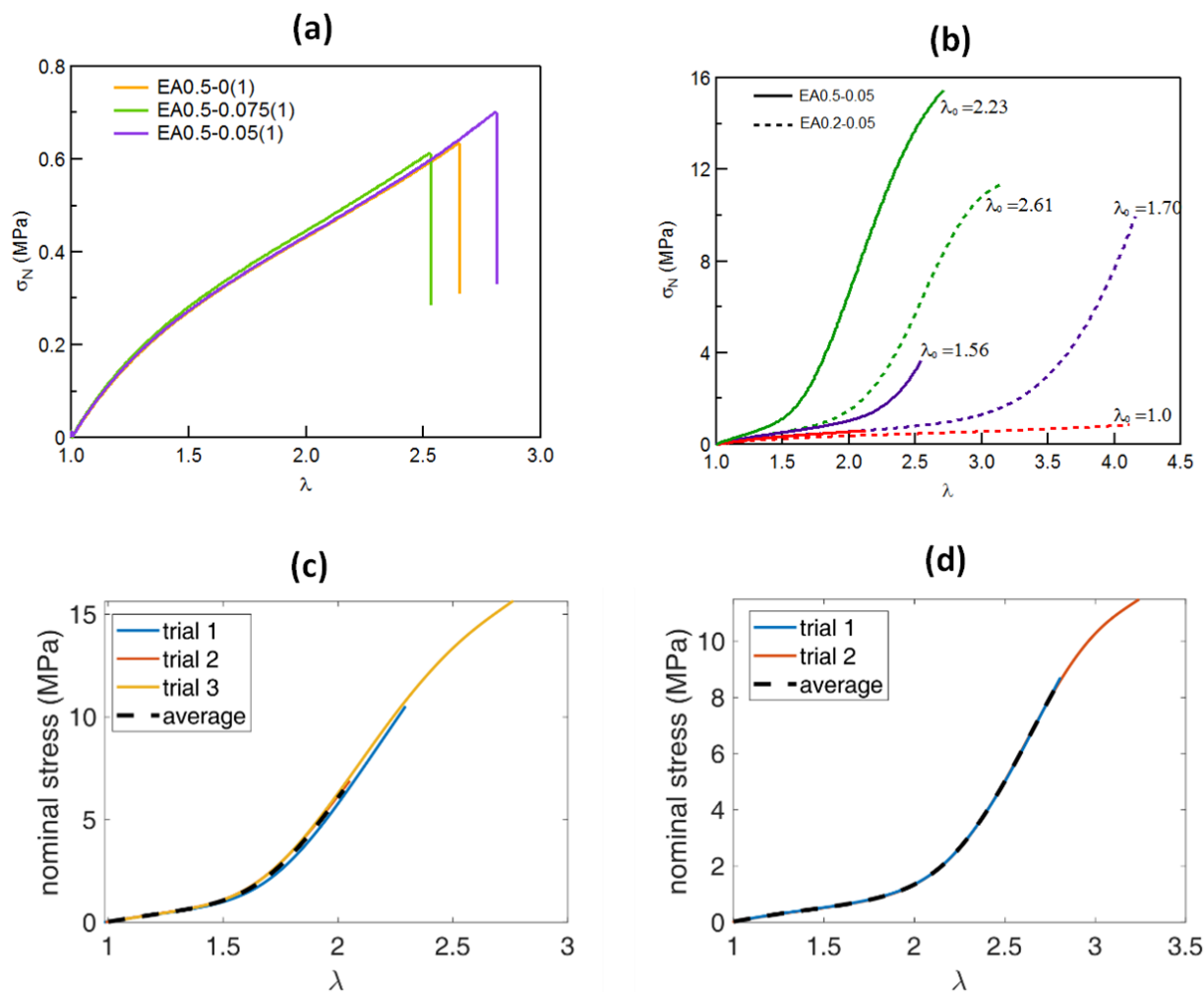


Figure S2: Stress-strain curves for different multiple network materials. (a) Stress-strain curves of various single networks with different concentrations of SP. The SP concentration in the three materials are 0, 0.05, and 0.075 mol% relative to EA monomers for the yellow, green, and purple lines, respectively. (b) Stress-strain curves of EA0.5-0.05 and EA0.2-0.05 families of materials. (c) Stress-strain curves for 3 different samples of EA0.5-0.05(2.23) material. (d) Stress-strain curves for 2 separate samples of the EA0.2-0.05(2.61) material.

The data presented are based on the standard EA0.5-0.05 family of materials, which contains the same SN concentration. To ensure reliability, triplicate measurements were performed for each specimen type. The main results of the mechanical tests are shown in Table S2. The increase in Young's modulus and maximum stress shows the typical reinforcement effect observed for multiple networks.

Table S2: Mechanical properties of EA0.5-0.05 family of multiple network elastomers.

Sample name	λ_0	SN wt%	N_{poly}	E (MPa)	Stress at break (MPa)
EA0.5-0.05(1)	1	100	1	0.85±0.016	0.9±0.28
EA0.5-0.05(1.56)	1.56	26.5	2	1.21±0.027	4.6±0.16
EA0.5-0.05(2.23)	2.23	9.0	3	1.99±0.090	15.3±0.14
EA0.2-0.05(1)	1	100	1	0.62±0.056	0.8±0.06
EA0.2-0.05(1.70)	1.70	20.2	2	0.98±0.117	8.7±1.37
EA0.2-0.05(2.61)	2.61	5.6	3	1.32±0.081	9.8±2.06

The stress-strain curves of the EA0.5-0.05 and EA0.2-0.05 families of elastomers are shown in *Figure S2a*. The SNs shows a typical neo-Hookean behavior until fracture at around 200% extension, DNs display initial strain hardening before fracture, and TNs possess a strain hardening and strain softening behavior leading to a high stress at break, as shown in *Figure S2b*. Comparing the stress-strain curves of the EA0.5-0.05 and EA0.2-0.05 families, the reduction in cross-linker density of the filler network resulted in a decrease in the modulus with no decrease in the observed nominal stress at break. Also, the EA0.2-0.05 family of materials was more extensible than the EA0.5-0.05 family.

2.2 Fracture tests

Fracture tests were performed with the TNs in the EA0.2-0.05 and EA0.2-0.05 material families. A uniform rectangular sample was made by a strip punch with a length of 20 mm and a width of 10 mm. A 1 mm notch was made with a razor blade on one side of the sample. The sample was fixed on the pneumatic clamps and the original length of the sample between clamps was set at around 10 mm. The video camera recorded the mechanical response during the fracture test at a stretch rate of $\dot{\lambda} = 0.05 \text{ s}^{-1}$. The recorded videos were used to accurately measure the extension by tracking two dots (two marks or two surface features) using a MATLAB script. The critical stretch, λ_c , prior to crack propagation was measured and used to calculate the strain energy density $W(\lambda_c)$ by integrating the stress-strain curves of un-notched samples up to λ_c . The fracture energy, Γ , is equal to the energy release rate \mathcal{G} when the critical stretch is reached, i.e., $\lambda = \lambda_c$. Using the Greensmith relation (35) in Equation 2 of the main text:

$$\Gamma = \frac{6}{\sqrt{\lambda_c}} \times W(\lambda_c) \times c, \quad \text{Eq. S2}$$

where c is the notch length. To obtain an accurate calculation of Γ , an average of the stress-strain response for the unnotched samples were used, as shown in *Figure S2c* and *Figure S2d*.

3 Color analysis

3.1 Information obtained from RGB video data

Uncompressed raw video footage was recorded using a SenTech (SONY IMX 174, STC-MCS241U3V) RGB CCD camera. Photons in the visible light spectrum were captured by the camera sensors sensitive to red, green, or blue light. Collected photons were then converted to a voltage signal, which is recorded as a discretized 8-bit digital value. Photon counts are linearly proportional to the 8-bit value within a color channel, S :

$$S \propto \int_0^\infty N_p F_{IR} Q d\lambda, \quad \text{Eq. S3}$$

where N_p , F_{IR} , and Q represent the number of photons transmitted, the camera filter defining the visible spectrum, and the quantum efficiency of the sensor. For clarity, the variable, S , is herein used to generically represent any of the red (R), green (G), and blue (B) channels. The camera sensitivity, defined as the product of Q and F_{IR} , is shown in *Figure S3a*. The Beer-Lambert law can be applied to Eq. S3, which relates the absorption coefficient, ϵ , and the concentration, c , of the activated mechanophore and the sample thickness, t , to S :

$$S \propto \int_0^\infty e^{-\epsilon ct} F_{IR} Q d\lambda. \quad \text{Eq. S4}$$

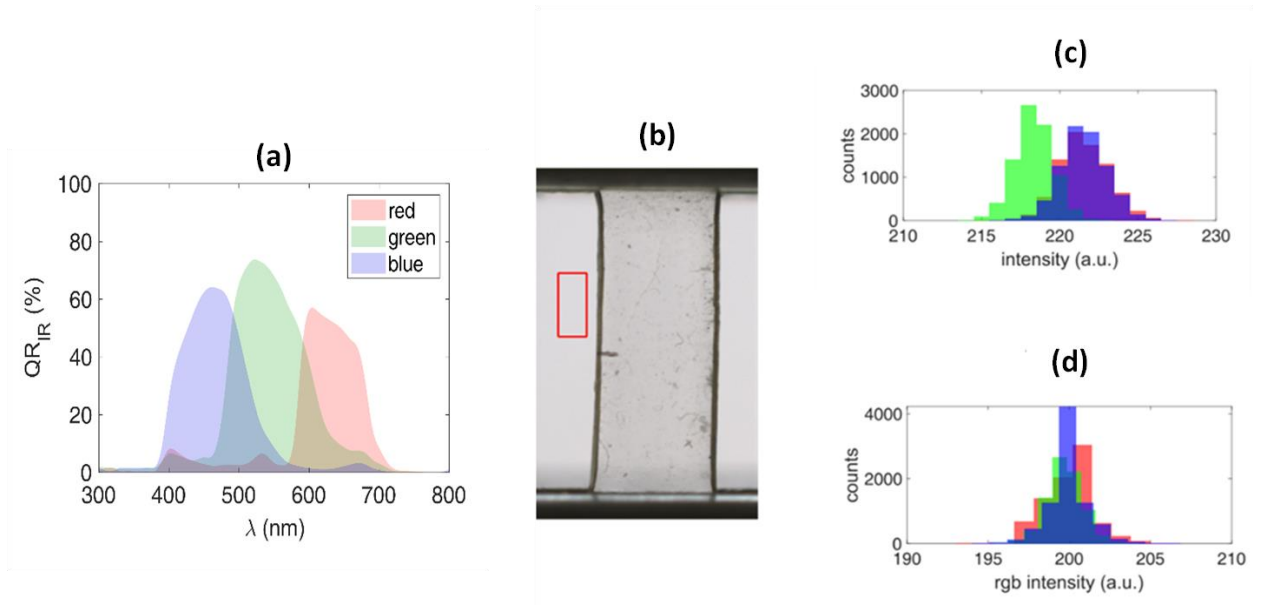


Figure S3: Background correction for color analysis. (a) The camera sensitivity spectrum in the visible range. Normalized values of the product of Q and F_{IR} for the SenTech STC-MCS241U3V RGB camera were obtained from (33) and the technical camera specifications provided by SenTech. (b) A representative area of the white background (shown in the red box) is used to determine, f_s (see Eq. S5). (c) An RGB histogram of that region before color correction. (d) An RGB histogram of the same region after color correction.

3.2 Image processing

Frames were extracted from the recorded uncompressed video. A static “white” background region as shown in Figure S3 was defined as a reference region for color correction. Intensities in each color channel were rescaled by a factor, f_s , so that the mean channel intensities, S_{mean} , in the white reference region matched an arbitrarily defined value, A :

$$f_s = \frac{A}{S_{mean}}. \quad \text{Eq. S5}$$

Note that A can be arbitrarily defined, since this constant cancels out when calculating chromaticity (see next section). Color correction was performed by applying the rescaling factors to the rest of the image frame. An example of the color correction is shown in Figure S3c and S3d. Image processing was performed using a script written in MATLAB 2017b (Mathworks, Natick, MA, USA).

3.3 Chromaticity

To perform quantitative color analysis, the red, green, and blue chromatic values were calculated for each pixel (33,36):

$$S_{ratio} = \frac{S}{\sum S}, \quad \text{Eq. S6}$$

where the color channel chromaticity is denoted by the subscript, *ratio*. By substituting Eq. S5 into Eq. S6, chromaticity can be expressed in terms of the color channel intensities prior to color correction:

$$S_{ratio} = \frac{S_0/S_{mean}}{\sum S_0/S_{mean}} \quad \text{Eq. S7}$$

where the subscript, “0”, denotes the channel intensity before color correction. As previously mentioned, the arbitrary constant defined in Eq. S5 cancels out in the definition of chromaticity. To provide a physical interpretation of the chromatic change, Eq. S4 can be substituted into Eq. S6:

$$S_{ratio} = \frac{\int_0^\infty e^{-\epsilon ct} F_{IR} Q_S d\lambda}{\int_0^\infty e^{-\epsilon ct} F_{IR} Q_R d\lambda + \int_0^\infty e^{-\epsilon ct} F_{IR} Q_G d\lambda + \int_0^\infty e^{-\epsilon ct} F_{IR} Q_B d\lambda}. \quad \text{Eq. S8}$$

Eq. S8 shows that chromaticity has the same non-linear dependence on both the sample thickness and merocyanine concentration. Thus, thickness effects should be decoupled from changes in concentration by performing experiments on a material system with the same initial sample thickness. Otherwise, chromaticity cannot be exclusively correlated with concentration, since the sample thickness will change during mechanical deformation due to the Poisson’s effect. To circumvent this issue, experiments performed on samples within the same family of materials were prepared with the same thickness.

Although normalized to the total intensity (or brightness) of the pixel, chromaticity is dependent on the relative ratios between the color channels in the white background. Therefore, it is important that experiments are performed under similar color-lighting conditions. To ensure that color-light conditions were similar, the white background histograms between the fracture and calibration experiments were compared and confirmed to be similar.

3.4 Sensitivity of the RGB camera towards SP activation

Elastomers with varying SP concentrations in their first networks were tested in uniaxial extension to examine the dependence of the chromatic change on SP concentration. Although the

three materials exhibit slightly different mechanical properties due to differences in prestretching of the first network as shown in *Figure S4a*, the absolute slope of the chromatic change plotted over either the strain or nominal stress decreases with the SP concentration. Also, the nominal stress or strain corresponding to the detection limit of the chromatic change (represented by the intersection between the red and blue chromatic changes and the boundary of the noise band in *Figure S4a* and *Figure S4b* increases as the SP concentration decreases. Altogether, the choice of using a SP concentration of 0.05 mol% is justified due to its lower nominal stress at the detection limit.

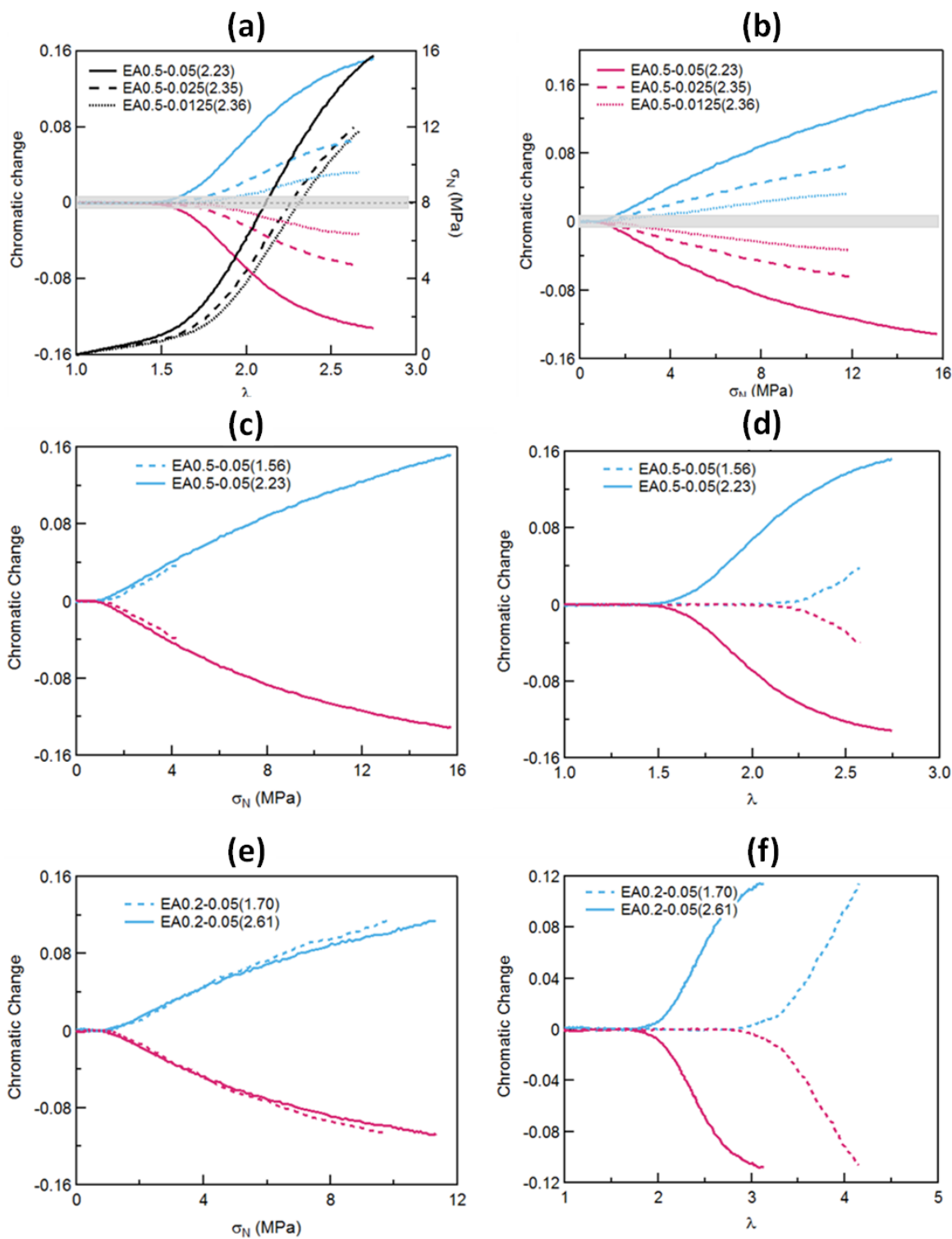


Figure S4: RGB analysis in uniaxial tension for three different materials. (a)-(b) RGB analysis in uniaxial tension for three different materials. The first network contains the same total crosslinker concentration but various SP concentration in the first network. (a)

Chromatic change and nominal stress plot as a function of stretch. (b) Chromatic change plots as a function of stress for the same materials as in (a). The gray regions represents the noise bands.

(c)-(f) RGB analysis in uniaxial tension for two families of materials derived from the same filler networks. (c) Chromatic change plot as a function of nominal stress and (d) Chromatic change plot as a function of stretch for the EA0.5-0.05 family. (e) Chromatic change plot as a function of nominal stress and (f) Chromatic change plot as a function of stretch for the EA0.2-0.05 family.

3.5 Chromatic change in families of materials

Families of elastomers deriving from the same filler network were synthesized and uniaxial extension tests were performed to measure their chromatic change. DNs (EA0.5-0.05(1.56) or EA0.2-0.05(1.70)) are softer and more extensible than TNs (EA0.5-0.05(2.23) or EA0.-0.05(2.61)) described in the main text due to the lower prestretch in the filler networks. The curves of chromatic change vs. stretch show a higher critical strain of chromatic change in these DN (*Figure S4d* and *Figure S4f*) than in the networks discussed in the main text. Above the critical strain the absolute value of chromatic change is also lower in DN than in TN. However, for both families of materials, if the chromatic change is plotted as a function of nominal stress (*Figure S4c* and *Figure S4e*), a master curve is clearly observed. These two master curves clearly show that SP acts as a stress sensor and not a stretch sensor.

3.6 Strain rate effects

Additional control tests on the effects of strain rate and spiropyran activation kinetics were carried out. Uniaxial tension tests were performed and video recorded on EA0.5-0.05(2.23) samples at different strain rates ranging from 0.01 s^{-1} to 0.1 s^{-1} , as shown in *Figure S5*. *Figure S5e* shows the stress-strain curves of EA0.5-0.05(2.23) at different stretch rates. No significant difference was observed from the curves (the same Young modulus and strain hardening phenomenon). This further confirms that viscoelastic effects due to chain entanglement have a negligible effect on the multiple network elastomers made from poly(ethyl acrylate) at room temperature. The videos captured during the tensile tests carried out at various stretch rates were used to perform color analysis and results are shown in *Figure S5* a and c. Although the materials show negligible viscoelasticity, the chromatic change had some strain rate dependence. At the same stress or first network extension, the higher strain rates resulted in a slightly lower

chromatic change. This rate dependence is attributed to a characteristic time associated with the SP activation, which is also observed by Craig et al. in the detection of the force to activate SP. The rate dependence of chromatic change was defined by referring to the chromatic change at the lowest stretch rate (0.01 s^{-1}), as shown in *Figure S5* b and d. The rate dependence leads to a maximum difference of about 10%. The results show that chromaticity due to SP activation has a weak dependence on strain rate. This implies that time dependence due to viscoelasticity and/or kinetics of mechanophore activation do not play an important role in sample color change under experimental conditions performed herein.

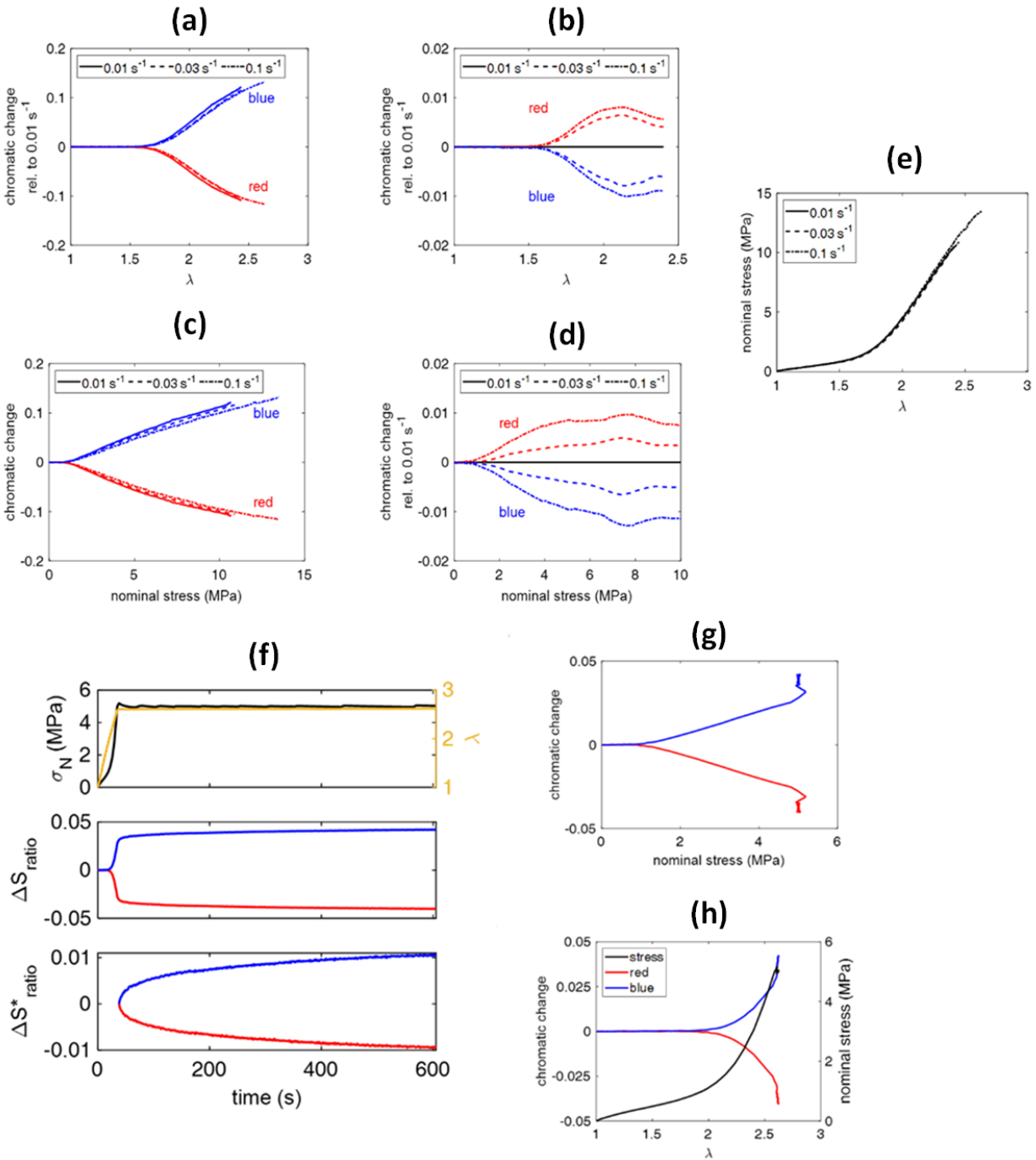


Figure S5: Strain rate effects on chromatic change. (a) Chromatic change as a function of the applied extension for three different strain rates. (b) Difference in chromatic change between the two higher strain rates and the chromatic change at 0.01 s⁻¹ as a function of the applied extension. (c) Chromatic change as a function of the nominal stress for three different strain rates. (d) Difference in chromatic change between the two higher strain rates and the chromatic change at 0.01 s⁻¹ as a function of the nominal stress. (e) Stress-extension curves at 0.01, 0.3, and 0.1 s⁻¹. Tests at different strain rates were performed on EA0.5-0.05(2.23) samples. (f) σ_n (black) and λ (yellow) values as a function of time (top), chromatic change, ΔS_{ratio} , as a

function of time (middle), and chromatic change after reaching the target stress of 5 MPa, ΔS_{ratio}^* , as a function of time (bottom). (g) Chromatic change as a function of nominal stress. (h) Chromatic change as a function of λ . The creep test was performed on a EA0.2-0.05(2.61) sample.

Spiropyran activation kinetics were also examined for an EA0.2-0.05(2.61) sample subjected to a constant load of 5 MPa for 10 min. using an Instron machine under force-control settings. As shown in *Figure S5a* to *Figure S5h*, the absolute chromatic change relative to reaching the target stress of 5 MPa correspond to a value of ~ 0.01 after 10 min. Most of the change in chromaticity ($\pm \sim 0.005$) occurred during the first 100 s of the experiment or ~ 50 s after reaching the target stress. This rate of change is slow given the typical experimental time in uniaxial extension (~ 45 s) or fracture (~ 20 s) and the rate in which the signal systematically changes should be low. The deviation due to the time dependence can be estimated in the measurement of stress by color-stress calibration curve. According to the color calibration curve, the slope is about ± 1 MPa/0.01 for the blue or red chromatic change. At most, the maximum deviation of stress due to the rate or time dependent activation kinetics will lead to an increase of ~ 0.5 MPa. The deviation is not an essential effect on the detection of stress in the materials. Considering that the color change is not decreasing during the experiment, merocyanine was considered to be stable under constant load conditions. In other words, ambient white light does not play an important role in driving deactivation (conversion of merocyanine back to spiropyran) when the sample is under constant load.

In summary, results are consistent with what has been observed by Craig et al. However, the spiropyran activation kinetics was determined to have a relatively small effect on the rate of change in chromaticity at the experimental time frame of the mechanical tests.

4 Construction of the chromatic stress calibration

Two chromatic values are sufficient to describe color change and construct a 2D chromatic coordinate that can be used to trace the color evolution during a uniaxial tension experiment, as shown in *Figure S6a* and *Figure S6b*. Chromatic changes were calculated relative to the start of the experiment.

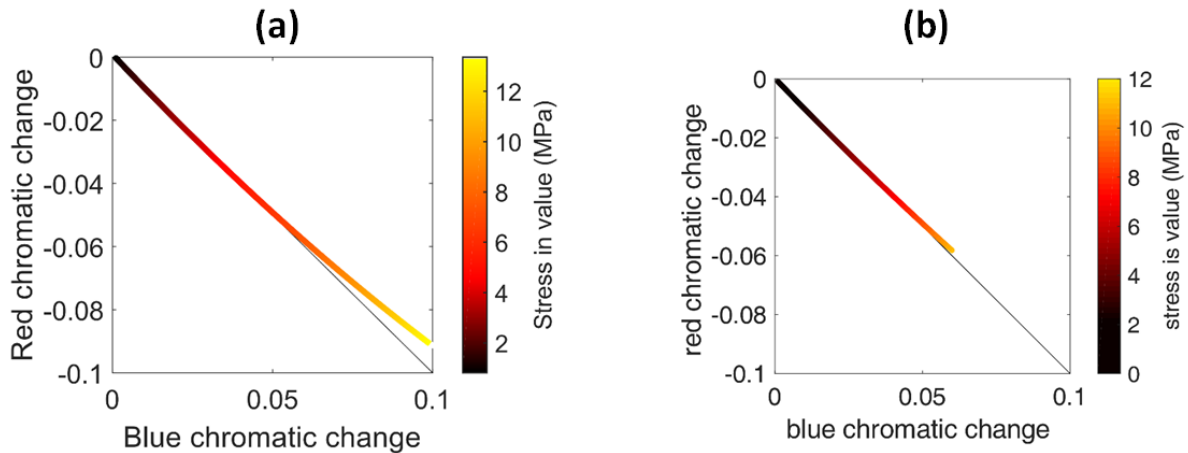


Figure S6: The calibration curves of stress vs. chromatic change. (a) Nominal stress is represented with a color map for each value of red and blue chromatic change for the (a) EA0.5-0.05(2.23) and (b) EA0.2-0.05(2.61) samples being pulled in uniaxial tension. Stress levels are represented by the colorbar. The dashed line serves as a reference line with a slope of -1.

The chromatic stress plot can be used to correlate a (uniaxial tension) stress value based on the chromatic state of a pixel in a sample experiencing a heterogenous stress state, such as that of a fracture experiment. However, application of the chromatic stress calibration requires careful treatment to properly account for experimental noise and data association along the chromatic stress curve. Also, to account for thickness differences between families of materials, a chromatic stress calibration was generated for each material family.

5 Constructing stress maps around a crack tip

Consider a single edge notch fracture experiment of a 5 mm wide rectangular sample as described earlier. The intrinsic chromatic noise in the sample can be characterized by extracting statistics in a representative region in the sample, as shown in *Figure S7*. By assuming that the chromatic changes can be characterized by Gaussian statistics, a signal to noise threshold can be systematically defined based on the number of standard deviations from the mean chromatic change (defined at 0). The red lines outlined in *Figure S7c* represent the noise level. (i.e. two standard deviations, where data lying outside this threshold can be interpreted as having a probability of less than 5% that the data is attributed to noise).

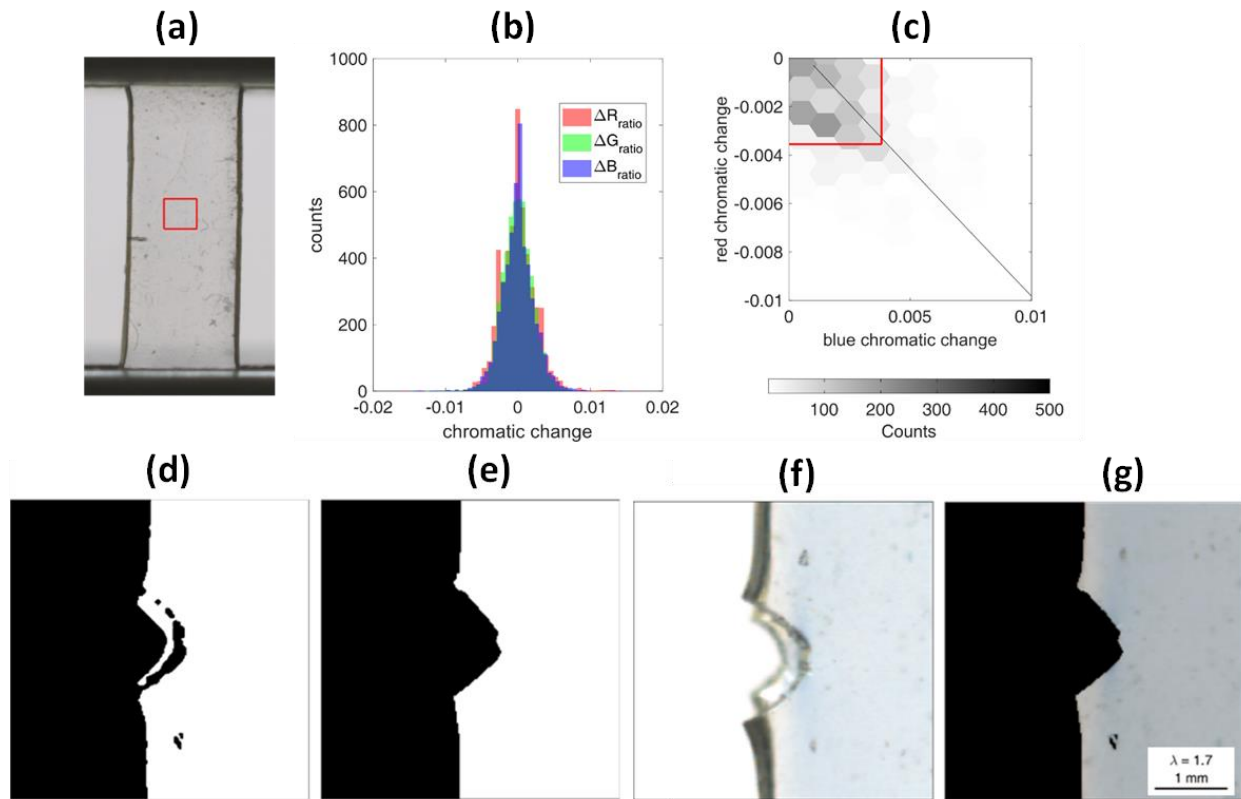


Figure S7: Analysis of the fracture images. (a) A representative sample region is defined prior to loading outlined by the red box. (b) A chromatic change histogram of the reference sample region. (c) A bivariate hexagonal histogram between red and blue chromatic changes. The red box represents two standard deviations from the mean chromatic change (set at 0). The solid black line traces the chromatic change evolution obtained from the calibration curve (see Figure S5). (d) Masking result of an EA0.5-0.05(2.23) fracture sample pulled to an extension ratio, λ , of 1.7 using the binary threshold method. (e) Additional manual masking modifications were performed so that color analysis was only applied at the front sample surface. (f) Color corrected image prior to masking. (g) The overlaid mask on top of the color corrected frame.

As the SP labeled fracture sample is uniaxially stretched, the sample will change color. To perform the color analysis only in the sample region, a mask was used to differentiate the foreground (the sample) from the background, as shown in Figure S7 d to Figure S7g. The masking procedure was guided by a binary thresholding method and additional manual modifications. Subsequent edits to the mask were performed so that the color analysis was only applied the front surface of the sample excluding sample edges. Note that masked regions in the middle of the sample due to sample defects were not additionally modified. By using this masking protocol, the mask excludes sample regions exhibiting tri-dimensionality in the crack

geometry, restricting the color analysis to the planar regions of the sample. In other words, the color analysis assumes homogeneity in the thickness direction.

5.1 Supplementary figures associated with the stress mapping of EA0.5-0.05(2.23) and EA0.2-0.05(2.61)

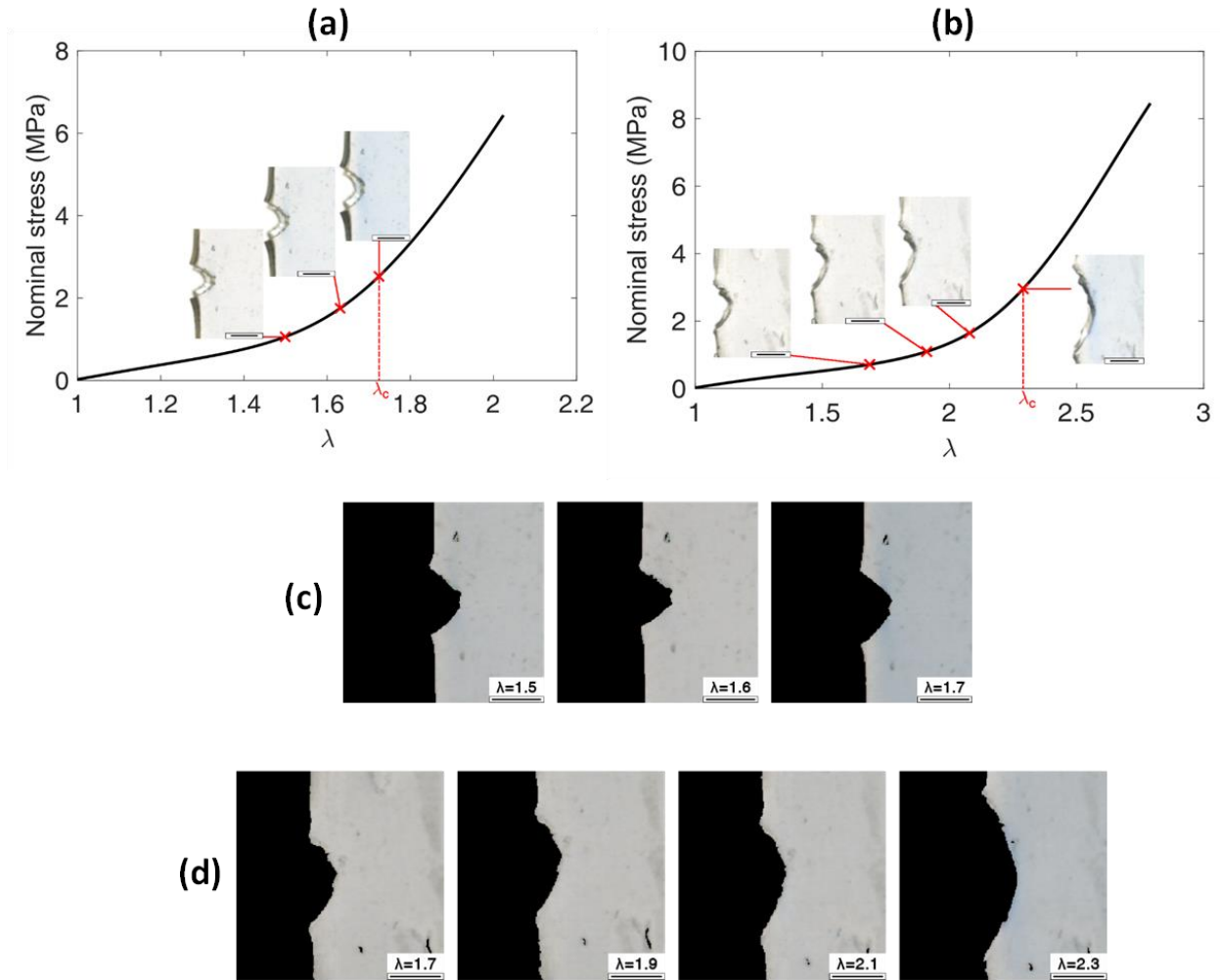


Figure S8: Background corrected images of fractures. (a) for the EA0.5-0.05(2.23) fracture sample and (b) for the EA0.2-0.05(2.61) fracture sample (from Figure 5 in the main paper) represented on the stress-strain curve of the unnotched sample. The horizontal bars on the images represent 1 mm. (c) Masks overlaid on top of the color corrected frames for the images of (a). (d) Masks overlaid on top of the color corrected frames for the images of (b).

In order to associate a stress value to each pixel we need to compare the chromaticity of the pixel to the calibration curve. This association to the calibration curve for each pixel with a signal above the chromatic signal to noise threshold was based on the minimum Euclidean distance between the noisy datapoint and the calibration curve, as illustrated in *Figure S9a*. This association was performed by implementing the MATLAB kd-tree `knnsearch` function in the MATLAB script. Once the associated chromatic coordinates have been identified, the stress was obtained from the chromatic stress calibration and each pixel was then attributed a value of stress, as shown in *Figure S9b*.

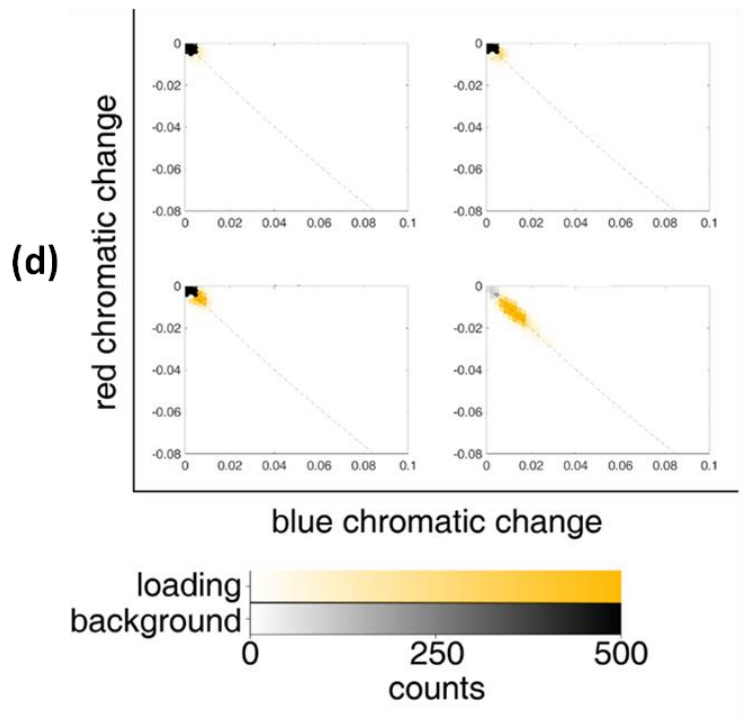
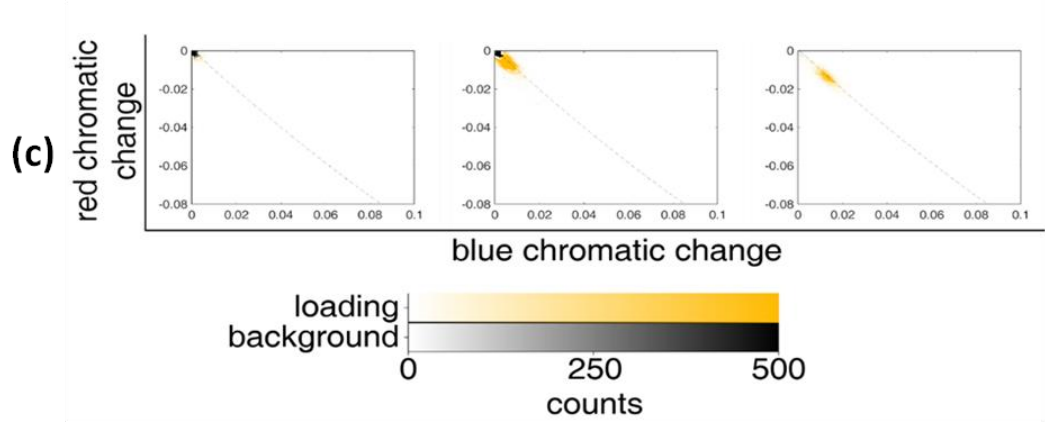
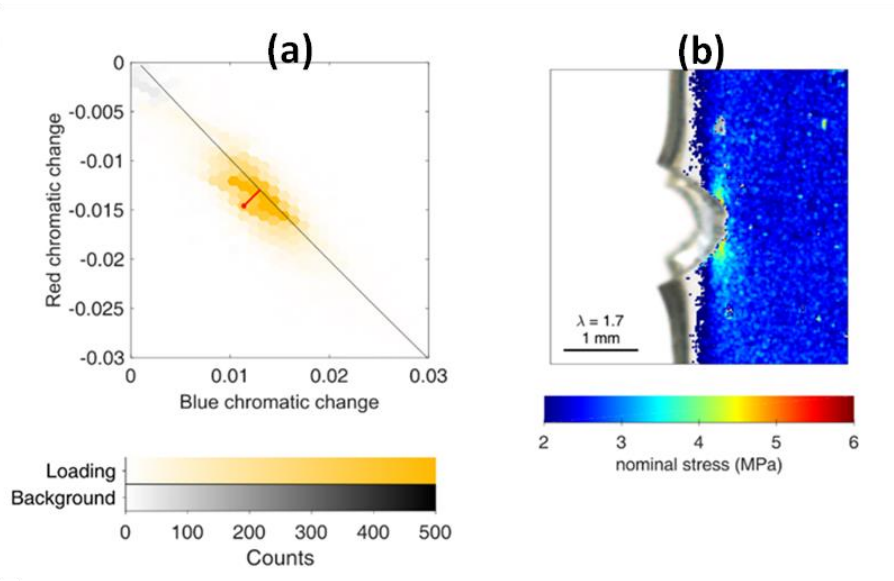


Figure S9: The mapping process of stress around crack tip. (a) A bivariate hexagonal histogram between red and blue chromatic changes. The red dot, representing a chromatic coordinate based on a pixel obtained from a fracture sample (see Figure S7 g), is associated to a point along the chromatic stress calibration curve, plotted as the black line, based on the shortest Euclidean distance, represented by the red line. Note that the histogram color categorizes pixels from the fracture sample as either background/baseline noise (black) or signal (yellow). The stress component of the chromatic stress calibration is not shown for clarity. (b) The deduced correlated stress for each pixel identified as signal mapped onto the color-corrected subimage frame. (c) and (d) bivariate hexagonal histogram between red and blue chromatic change for the EA0.5-0.05(2.23) fracture sample and the EA0.2-0.05(2.61) fracture sample. (c) and (d) correspond to frames in Figure S8 c and d, respectively.

6 Simulation

An incompressible Ogden model (39) was used to characterize the strain and stress response.

The Ogden strain energy potential U is expressed as,

$$U = \sum_{i=1}^N \frac{2\mu_i}{\alpha_i^2} (\lambda_1^{\alpha_i} + \lambda_2^{\alpha_i} + \lambda_3^{\alpha_i} - 3), \quad \text{Eq. S9}$$

in which $\lambda_k (k = 1,2,3)$ is the principal stretch, μ_i is the shear modulus and α_i is the parameter that governs the stiffening. Results show that $N = 2$ gives good fitting of the experimental uniaxial tensile test for both the EA0.5-0.05(2.23) and EA0.2-0.05(2.61) materials, as shown in *Figure S10a* and *Figure S10b*. Note that the experimental uniaxial test used for the fitting was based on the average unnotched stress-strain responses of 3 trials (see *Figure S2*). Under uniaxial tension, $\lambda_1 = \lambda, \lambda_2 = \lambda_3 = 1/\sqrt{\lambda}$, the nominal stress is expressed as the function of stretch ratio λ :

$$\sigma_N = \frac{2\mu_1}{\alpha_1} (\lambda^{\alpha_1-1} - \lambda^{-\alpha_1/2-1}) + \frac{2\mu_2}{\alpha_2} (\lambda^{\alpha_2-1} - \lambda^{-\alpha_2/2-1}). \quad \text{Eq. S10}$$

Fitting parameters for the EA0.2-0.05(2.61) and EA0.5-0.05(2.23) material are shown in *Table S3*.

Table S3: Fitting parameters used in the Ogden model for fitting uniaxial stress-strain responses of EA0.5-0.05(2.23) and EA0.2-0.05(2.61) materials.

Parameters	μ_1 / MPa	α_1	μ_2 / MPa	α_2
EA0.2-0.05(2.61)	1.854×10^{-2}	8.468	0.416	1.349
EA0.5-0.05(2.23)	0.131	8.638	0.515	-0.302

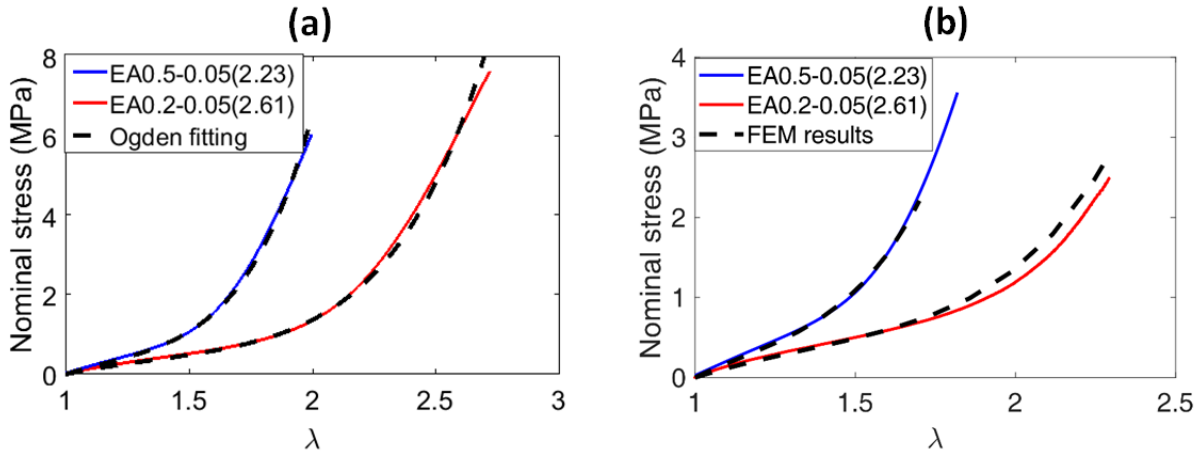


Figure S10: Fits of the stress-strain curves with the Ogden model. (a) The experimental data of nominal stress-stretch curves are fitted by using the Ogden model for the EA0.5-0.05(2.23) and EA0.2-0.05(2.61) materials. (b) Comparison between the FEM result and experiment data of global strain and average nominal stress of notched samples for the EA0.5-0.05(2.23) and EA0.2-0.05(2.61) materials.

To simulate the deformation and stress field of the Mode I crack, a 2D plane stress finite element model (FEM) in ABAQUS (v6.17, Simulia Inc., Providence, RI) was constructed. Geometry of the model was set the same as the fracture experiments, i.e., width $W = 5\text{mm}$, height $H = 10\text{mm}$, crack length $a = 0.75\text{ mm}$ for the EA0.5-0.05(2.23) sample and $a = 0.81\text{mm}$ for the EA0.2-0.05(2.61) sample. Due to symmetry, the FE model can be simplified as a half model with top surface loaded with uniform displacement and the bottom surface applied with symmetry

boundary. The model was meshed by 6200 CPS4 elements with smallest size equals to 0.01 mm. The bulk mechanical response was implemented by the Ogden model with the fitting parameter discussed above. The global stretch ratio versus the average stress (i.e., the applied force divided by the undeformed cross-section area) during the whole simulation was monitored. *Figure S10b* shows that the FEM result matches well with experimental data, indicating that the Ogden model can capture the mechanical behavior for both materials under multiaxial stress state. Therefore, the FE results can be used to compare with the experimental stress mapping determined from the chromatic stress mapping.

As discussed in the main text, the scalar stress obtained from the chromatic change of SP activation is interpreted as the maximum principal nominal stress. To relate this stress to the true stress obtained from FEM simulations, we note that the true stress tensor can be written as

$$\boldsymbol{\sigma} = \sum_{i=1}^3 \sigma_i \mathbf{n}_i \otimes \mathbf{n}_i, \quad \text{Eq. S11}$$

where σ_i are the principal true stresses (or eigenvalues of the true stress tensor $\boldsymbol{\sigma}$), \mathbf{n}_i are the corresponding principal directions and \otimes is the dyad notation. The nominal stress tensor $\boldsymbol{\sigma}_N$ i.e., the first Piola-Kirchhoff stress tensor, is related to the true stress tensor through the following equation¹⁷

$$\mathbf{S} = \boldsymbol{\sigma} \mathbf{F}^{-T} / \det(\mathbf{F}), \quad \text{Eq. S12}$$

where \mathbf{F} is the deformation gradient tensor. The incompressibility assumption implies that $\det(\mathbf{F}) = 1$. In addition, the Polar decomposition theorem dictates that

$$\mathbf{F} = \mathbf{V} \mathbf{R}, \quad \text{Eq. S13}$$

where \mathbf{V} is the left stretch tensor and \mathbf{R} is an orthogonal tensor describing the rotation component of \mathbf{F} . The left stretch tensor \mathbf{V} can be written in terms of the principal stretches λ_i as:

$$\mathbf{V} = \sum_{i=1}^3 \lambda_i \mathbf{n}_i \otimes \mathbf{n}_i, \quad \text{Eq. S14}$$

Substituting Eq. S11, Eq. S13 and Eq. S14 into Eq. S12, we find

$$\mathbf{S} = \boldsymbol{\sigma} \mathbf{V}^{-1} \mathbf{R} = [\sum_{i=1}^3 (\sigma_i / \lambda_i) \mathbf{n}_i \otimes \mathbf{n}_i] \mathbf{R} = \sum_{i=1}^3 (\sigma_i / \lambda_i) \mathbf{n}_i \otimes (\mathbf{R}^T \mathbf{n}_i). \quad \text{Eq. S15}$$

According to the kinematics of nonlinear elasticity (41), \mathbf{n}_i are the eigenvectors of the left Cauchy-Green tensor $\mathbf{F} \mathbf{F}^T$, and $\mathbf{N}_i \equiv \mathbf{R}^T \mathbf{n}_i$ or $\mathbf{R}^{-1} \mathbf{n}_i$ are the eigenvectors of the right Cauchy-Green tensor $\mathbf{F}^T \mathbf{F}$. Therefore, Eq. S15 can be finally written as

$$\mathbf{S} = \sum_{i=1}^3 (\sigma_i / \lambda_i) \mathbf{n}_i \otimes \mathbf{N}_i = \sum_{i=1}^3 S_i \mathbf{n}_i \otimes \mathbf{N}_i, \quad \text{Eq. S16}$$

where $S_i \equiv \sigma_i / \lambda_i$ are defined as the principal nominal stresses. Therefore, the maximum principal nominal stress (tensile) is equal to $\sigma_{\max} / \lambda_{\max}$.

As shown in Fig.6 of the main text, the field of $\sigma_{\max} / \lambda_{\max}$ predicted by the 2D plane stress FEM results achieves its maximum in a region directly ahead of the crack tip, while the experimental stress map measured from chromatic change reaches the maximum in a region on the crack surface (i.e., slightly on the left of the crack tip). This deviation is attributed to the fact that the crack front is not strictly perpendicular to the surface plane of the sample, but is tilted relative to the sample surface. To demonstrate this possibility, we built a three-dimensional (3D) FEM model in ABAQUS as shown in *Figure S11*. The lateral dimension of the 3D model was set to be the same as the 2D model, i.e., width $W = 5\text{mm}$ and height $H = 10\text{mm}$ (see *Figure S11a*). The thickness t_0 was estimated to be 1mm. Symmetry allowed us to simplify the 3D FEM model to a half of the sample geometry. Unlike the 2D model, the crack front was assumed to be a tilted line on the mid-plane of the sample, which results in different crack lengths on the front and back surfaces of the sample (see *Figure S11b*). On the front surface, which is the surface facing the camera in experiments, the crack length a_f was set to the same as that in the corresponding 2D model, i.e., $a_f = 0.75\text{mm}$ for the EA0.2-0.05(2.61) sample and $a_f = 0.81\text{mm}$ for the EA0.5-0.05(2.23) sample. On the back surface, it was estimated that the crack length a_b was 0.3mm less than a_f , i.e., $a_b = 0.45\text{mm}$ for the EA0.2-0.05(2.61) sample and $a_b = 0.51\text{mm}$ for the EA0.5-0.05(2.23) sample. The 3D FEM model was meshed by hybrid hexahedral elements (C3D8H) with the minimum mesh size being 0.01mm, which resulted in 355,888 elements for the EA0.2-0.05(2.61) sample and 349,856 elements for the EA0.5-0.05(2.23) sample. The three-dimensionality of the crack profile led to non-uniform $\sigma_{\max} / \lambda_{\max}$ along the thickness direction, as illustrated in *Figure S11c-e*.

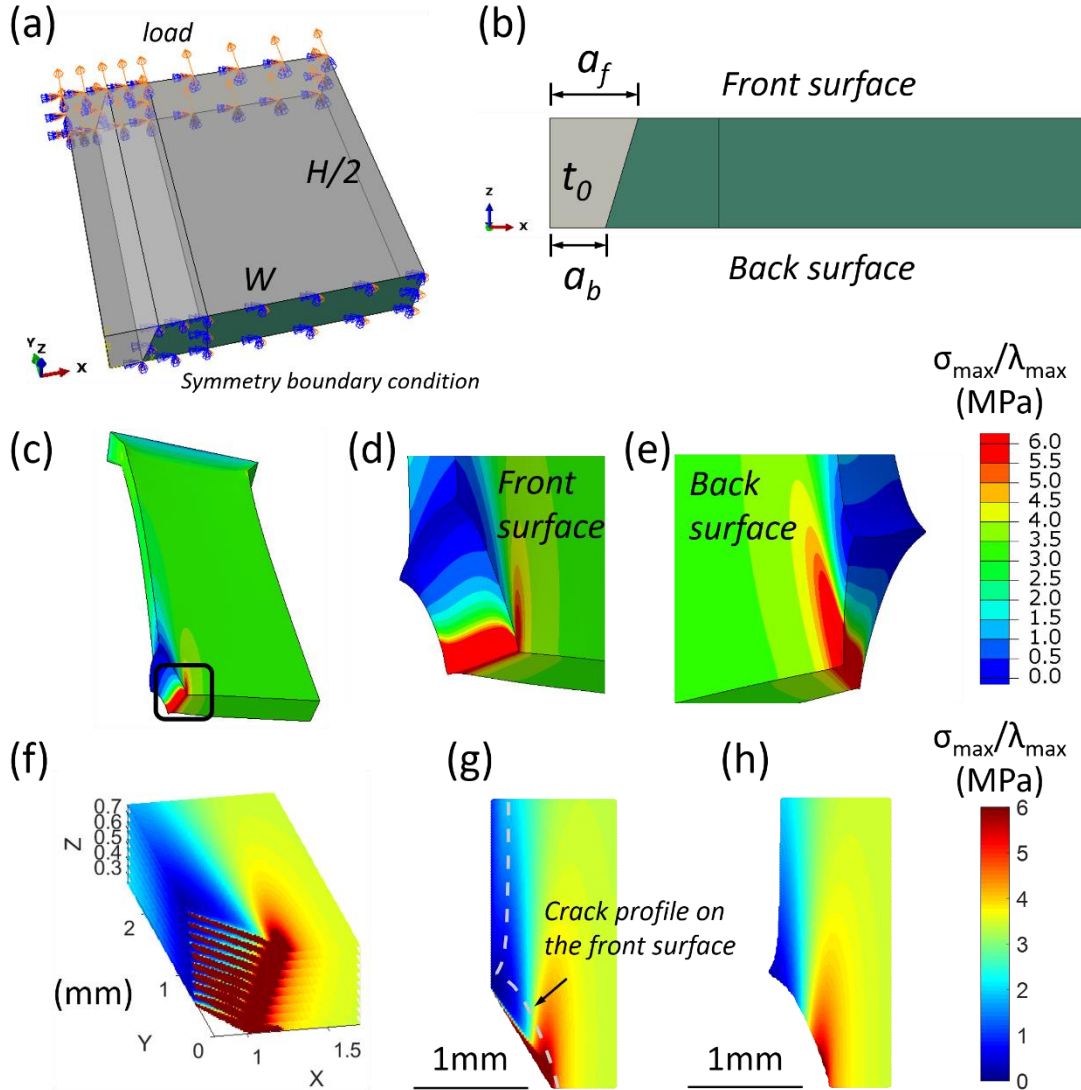


Figure S11: FEM model to account for 3D effects close to the crack tip. (a) Geometry of the 3D FEM model. (b) Mid-plane of the 3D FEM model showing that the crack front is a tilted line, which results in different crack lengths on the front and back surfaces. (c) 3D contour of $\sigma_{\max}/\lambda_{\max}$ in the deformed configuration for the EA0.2-0.05(2.61) sample. (d-e) Zoomed-in view near the crack front showing the top and bottom surfaces. (f) Contours of $\sigma_{\max}/\lambda_{\max}$ on ten planes perpendicular to the thickness direction in the deformed configuration obtained by interpolating the nodal values of $\sigma_{\max}/\lambda_{\max}$. Note that the deformed sample thickness is less than 1mm because of the contraction due to the Poisson's effect. (g) Contour of $\sigma_{\max}/\lambda_{\max}$ obtained by averaging the ten planes. The dashed line illustrates the deformed boundary on the front surface. (h) Projection of the average $\sigma_{\max}/\lambda_{\max}$ on the front surface.

The stress map measured from chromatic change reflects the averaged response across the sample thickness. To facilitate comparison with experimental data, we calculate the average value of $\sigma_{\max}/\lambda_{\max}$ across the thickness of the 3D FEM model and project the average stress

contour on the front surface. This procedure is implemented as follows. First, we collect data of $\sigma_{\max}/\lambda_{\max}$ at the nodes of the 3D FEM model and the corresponding nodal coordinates and wrote these data in “.txt” files using a Python script. These data files were read into MATLAB, where a seed grid was generated with 10 planes along the thickness direction and a spacing of 0.01mm within each plane. The function “griddata” in MATLAB was then used to obtain values of $\sigma_{\max}/\lambda_{\max}$ by linear interpolation based on the nodal data incorporated from the 3D FEM model (see *Figure S11f*). The values of $\sigma_{\max}/\lambda_{\max}$ on the 3D grid were converted into a 2D contour (see *Figure S11g*) by averaging the 10 planes along the thickness direction. Finally, the averaged 2D contour was projected onto the front surface by cropping out the regions outside the deformed boundary of the front surface, because in experiments only the pixels on the front surface of the sample were analyzed. This procedure leads to the contour of $\sigma_{\max}/\lambda_{\max}$ shown in *Figure S11h*.

Using the 3D FEM model and the procedure of averaging through thickness, we regenerated the predicted stress map of $\sigma_{\max}/\lambda_{\max}$ as shown in *Figure S12*. Also included in *Figure S12* are the experimental stress maps for comparison. It is seen that by implementing a tilted crack front, the peak stress region was shifted from directly ahead of the crack tip (i.e., the 2D plane stress FEM result in Fig.6) to slightly behind the crack tip (i.e., the 3D FEM result in *Figure S12*). Both the location and magnitude of the peak stress region agree well with those found in the experimental stress maps.

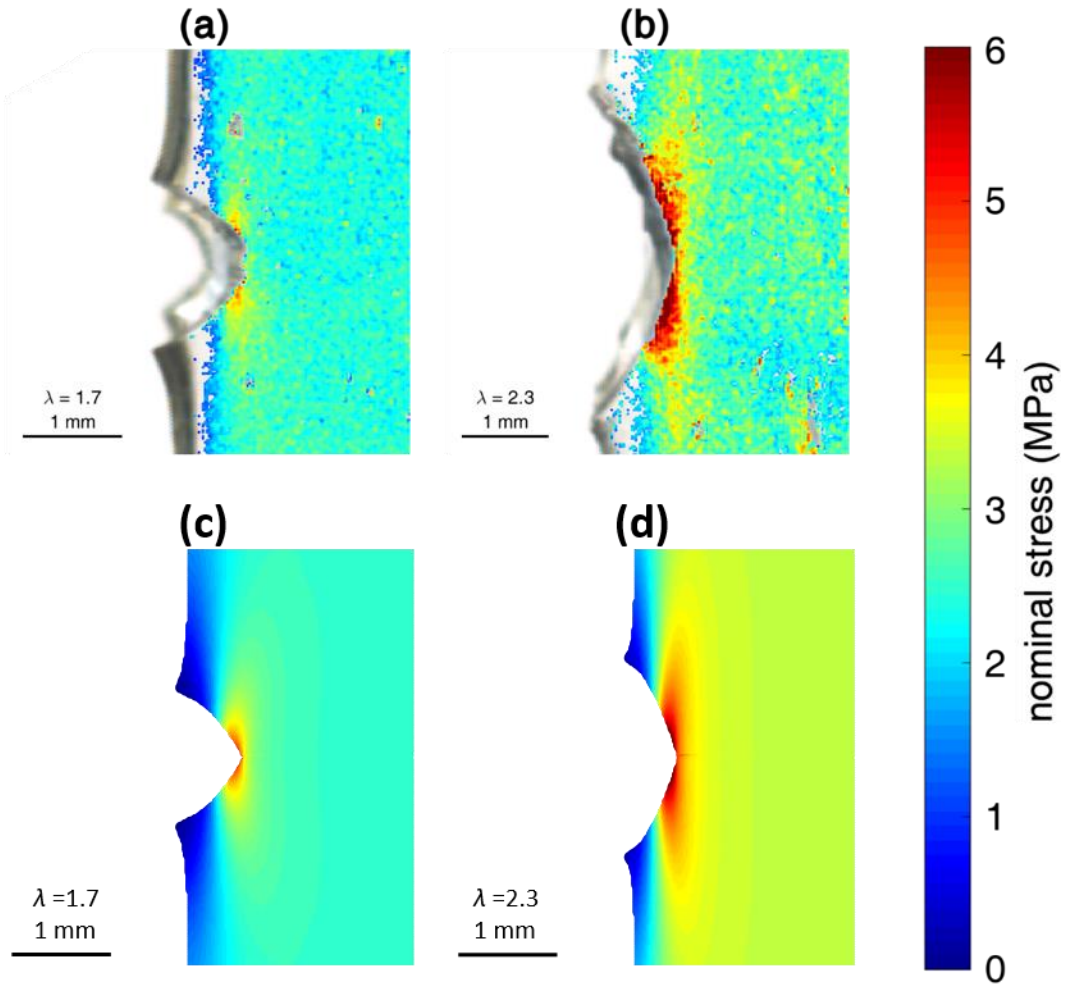


Figure S12: Comparison of experimental stress maps and simulated ones based on the 3D FEM model. The experimentally obtained stress map of (a) the EA0.5-0.05(2.23) and (b) the EA0.2-0.05(2.61) fracture samples. The simulated stress map of (c) the EA0.5-0.05(2.23) and (d) the EA0.2-0.05(2.61) fracture samples based on the 3D FEM model.